Annales
Geophysicae

Different Alfvén wave acceleration processes of electrons in substorms at ~4–5 R_E and 2–3 R_E radial distance

P. Janhunen, A. Olsson, J. Hanasz, C. T. Russell, H. Laakso, and J. C. Samson

Finnish Meterological Institute, Department of Geophysics, P.O. Box 503, 00101 Helsinki, Finland

Abstract. Recent statistical studies show the existence of an island of cavities and enhanced electric field structures at 4–5 R_E radial distance in the evening and midnight magnetic local time (MLT) sectors in the auroral region during disturbed conditions, as well as ion beam occurrence frequency changes at the same altitude. We study the possibility that the mechanism involved is electron Landau resonance with incoming Alfvén waves and study the feasibility of the idea further with Polar electric field, magnetic field, spacecraft potential and electron data in an event where Polar maps to a substorm over the CANOPUS magnetometer array. Recently, a new type of auroral kilometric radiation (AKR) emission originating from ~2–3 R_E radial distance, the so-called dot-AKR emission, has been reported to occur during substorm onsets and suggested to also be an effect of Alfvénic wave acceleration in a pre-existing auroral cavity. We improve the analysis of the dot-AKR, giving it a unified theoretical handling with the high-altitude Landau resonance phenomena. The purpose of the paper is to study the two types of Alfvénic electron acceleration, acknowledging that they have different physical mechanisms, altitudes and roles in substorm-related auroral processes.

Key words. Magnetospheric physics (storms and substorms; auroral phenomena) – Space plasma physics (wave-particle interactions)

1 Introduction

It has been suggested many times in the literature that kinetic or inertial Alfvén waves, because of their associated parallel electric field component, play a role in auroral electron acceleration (Hasegawa, 1976; Lysak and Carlson, 1981; Haerendel, 1983; Seyler, 1990; Hui and Seyler, 1992; Streltsov and Lotko, 1999; Lysak and Song, 2003a,b). In this paper we concentrate on transient Alfvénic waves arriving rather rapidly from the magnetosphere, not long-lived field-line

resonances that may explain some stable arcs (Samson et al., 2003). Since the ability of an Alfvén wave to accelerate electrons depends on the magnitude of its parallel electric field, which is significant only when the perpendicular wavelength is not much larger than the local electron inertial length, small-scale auroral arcs in particular, (1–2 km or less in the ionosphere) may be created by such waves. It has been pointed out by Wygant et al. (2000) that, at least in some substorm events, the Poynting flux carried downward by plasma sheet boundary layer Alfvén waves is enough to power the substorm-related bright auroras.

While the ability of an inertial Alfvén wave to accelerate electrons is well established theoretically, at least in a homogeneous plasma, much less is known observationally about where (what altitude) and when (substorm-related, active or all auroras) Alfvén-wave electron acceleration takes place and how important it is relative to other processes (potential structure related acceleration) in each case. Wygant et al. (2002) found evidence of Alfvén wave induced electron energisation at high altitude (4–6 R_E radial distance) during substorms. By radial distance we mean the geocentric distance and by altitude the distance measured from the surface of the Earth. In the 2–3 R_E radial distance range, Genot et al. (2000) showed, using simulations, that Alfvén waves incident on a pre-existing auroral cavity with sharp boundaries effectively become inertial Alfvén waves with perpendicular wavelength of the order of the gradient scale length of the boundary, resulting in significant parallel electric fields that are able to accelerate electrons. Further below, at about 4000 km altitude, electron precipitation that has been interpreted as resulting from Alfvén wave acceleration has been observed by FAST (Chaston et al., 2002), although the altitude of the acceleration is not given by these observations. Finally, at Freja altitude (~1700 km), it was found that Alfvén waves may participate in wave-particle interactions and in some cases carry significant Poynting flux (Louarn et al., 1994; Stasiewicz et al., 1998).
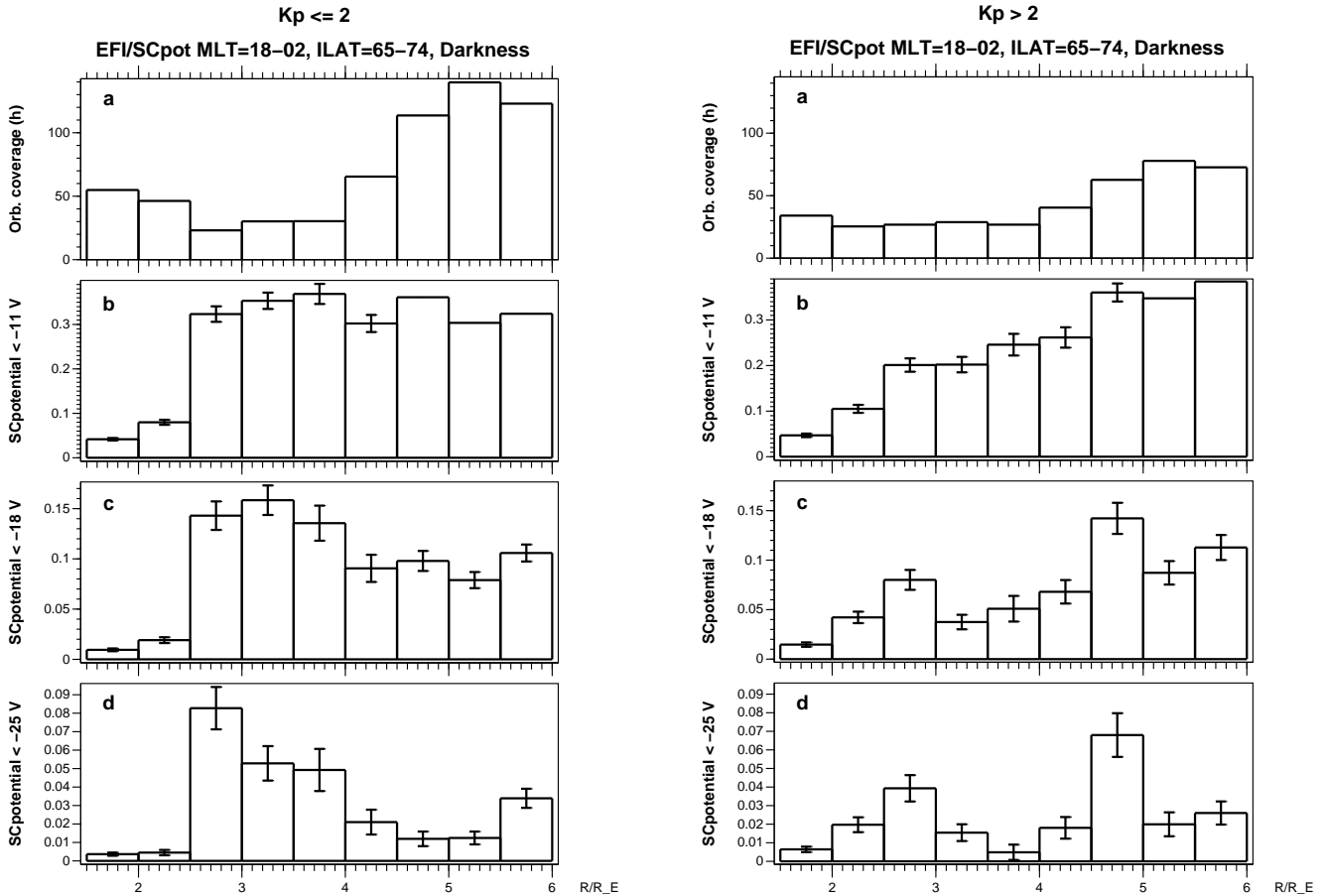
Fig. 1. Occurrence frequency of auroral cavities as determined from 5 years of Polar EFI spacecraft potential data in the 18–02 MLT range for conditions when the ionospheric footpoint is in darkness. Left plot is for $K_p \leq 2$ and right plot for $K_p > 2$. The top panel is the orbital coverage in hours while the remaining panels give the occurrence frequency for spacecraft potential thresholds -11 V, -18 V and -25 V. The horizontal axis is the radial distance from 1.5 to 6 R_E.

Recently, several large statistical studies using Polar data have been completed that also shed some light on the Alfvén wave acceleration question. The occurrence frequencies of auroral density depletions (Janhunen et al., 2002) and electric field structures (Janhunen et al., 2004a) show an interesting altitude dependence: the existence of separate low-altitude (2–3 R_E radial distance) and high-altitude (4–5 R_E radial distance) islands of density depletions and electric field structures. The high-altitude island occurs only during magnetically disturbed conditions ($K_p > 2$) and mainly in the midnight sector (22–02) and to a somewhat lesser extent in the evening (18–22) MLT sector. Also, the ion beam occurrence frequency changes at these altitudes (Janhunen et al., 2003). Thus, based on these statistical properties, the high-altitude island is probably substorm-related. Its likely relationship with Alfvén waves comes from the fact that the Alfvén speed at the high-altitude island is comparable to a typical electron thermal speed: if Alfvén waves are in Landau resonance with electrons somewhere in the magnetosphere, the most likely place is 4–5 R_E radial distance, which is exactly where

the substorm-related density cavity and its associated electric field structures are seen statistically. In this paper we call this region the Alfvén resonosphere (ARS). It is one of the purposes of this paper to elaborate on the ARS idea and to test it using both calculations and observational data.

A peculiar type of low-frequency auroral kilometric radiation (AKR) emission, the so-called "dot-AKR" emission (Hanasz et al., 2001; de Feraudy et al., 2001; Olsson et al., 2004), has been identified during substorms. The dot-AKR emission originates nearly at the same 2–3 R_E radial distance as the above-mentioned low-altitude density depletion island. It was suggested that the dot-AKR emission is a result of Alfvén waves becoming more inertial when passing through the low-altitude density depletion and thus accelerating electrons locally (Olsson et al., 2004). In this paper we also include the low-altitude region in the numerical model and give an improved handling of it so that the dot-AKR associated Alfvénic acceleration can be studied together with the high-altitude acceleration mentioned in the previous paragraph.
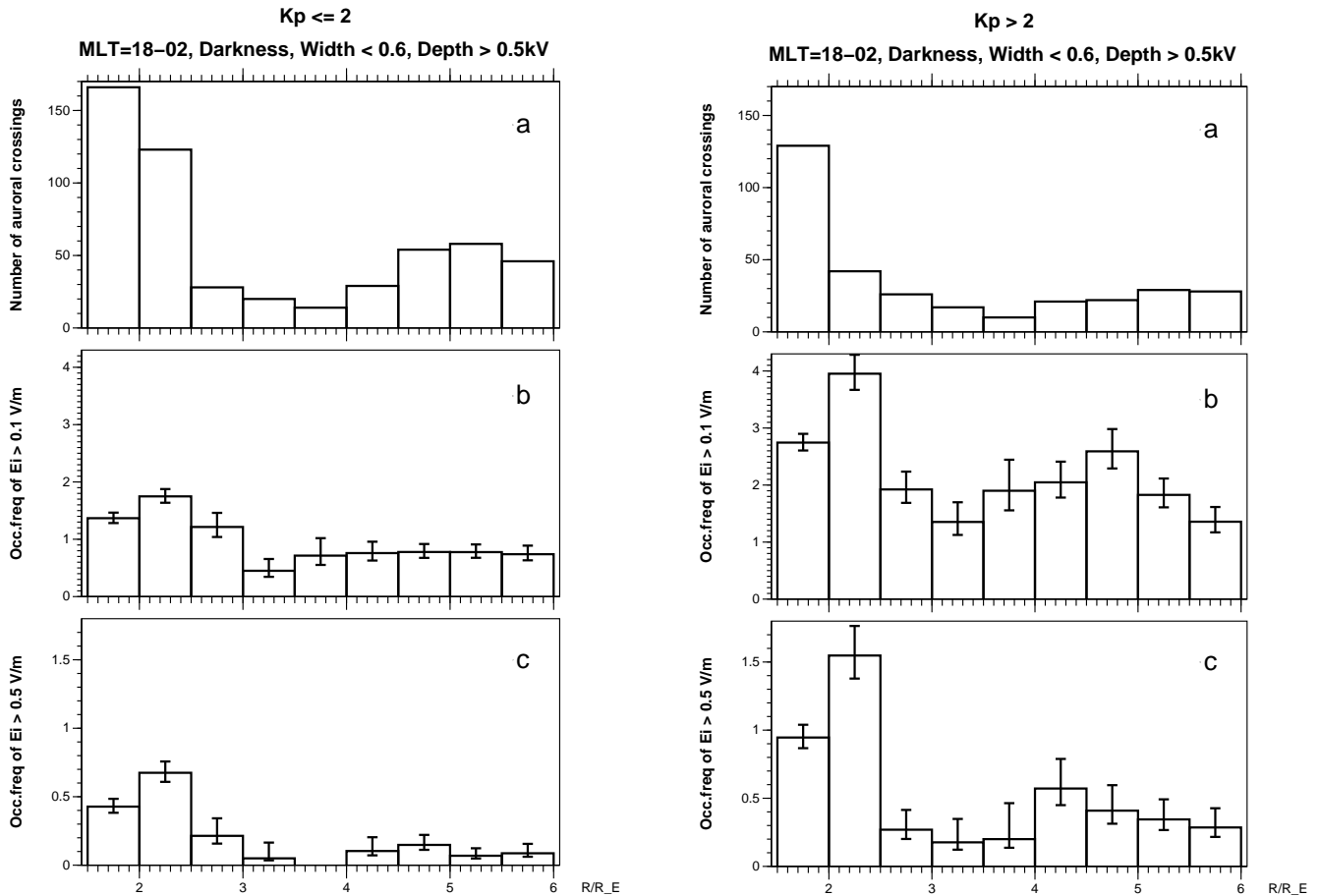
Fig. 2. From five years of Polar/EFI data: auroral potential minima deeper than 0.5 kV in 18–02 MLT range and the corresponding effective ionospheric electric fields E_i when the ionospheric footpoint is in darkness: **(a)** number of auroral crossings in each radial bin, **(b)** occurrence frequency of E_i being larger than 100 mV/m, **(c)** occurrence frequency of E_i being larger than 500 mV/m. Left plot is for $K_p \leq 2$ and right plot for $K_p > 2$. Only structures whose ionospheric width is smaller than $0.6°$ (~ 60 km) are included.

2 Statistical review results on density cavities, electric fields, ion beams and dot-AKR as a function of altitude

Polar satellite data have previously been used for studying how auroral density cavity (Janhunen et al., 2002), effective ionospheric electric fields (Janhunen et al., 2004a), ion beams (Janhunen et al., 2003) and dot-AKR (Olsson et al., 2004) statistically vary with radial distance (1.5–6 R_E). The density cavity study employed spacecraft potential data from the EFI instrument. The electric field study used EFI as well. The amount of EFI data used in both studies was about five years. The ion beam study used about two years worth of Polar/TIMAS data and a DE-1/EICS data set that spanned 11 years. The dot-AKR study used two years worth of data from the Polar/PWI wave instrument. During conditions when the ionospheric footpoint is in darkness, the statistics at low altitude (2–3 R_E radial distance) showed a density cavity and corresponding increase in the effective electric field during

both disturbed ($K_p > 2$) and quiet ($K_p \leq 2$) conditions, while at high altitude (4–5 R_E radial distance) the occurrence frequency was found to be very different during disturbed conditions when compared to quiet. Below we will show the resulting statistics for the auroral cavity (Fig. 1), the electric fields (Fig. 2) and the ion beams (Fig. 3) for conditions when the ionospheric footpoint is in darkness in 18–02 MLT. The left panels in all the figures are for magnetically quiet conditions and the right panels are for disturbed. The horizontal axis is the radial distance from 1.5 to 6 R_E. In Fig. 4 we show the emission radial distance statistics are that are deduced from Polar/PWI observed dot-AKR events during winter months. Since dot-AKR is associated with substorm onsets, all data points are under magnetically disturbed conditions. The statistical results below 4 R_E have previously been analysed in detail and interpreted as a result of a closed potential structure with an associated deep density cavity related to stable auroral arcs (Olsson and Janhunen, 2004). The dot-AKR emission was linked with deep cavities related to
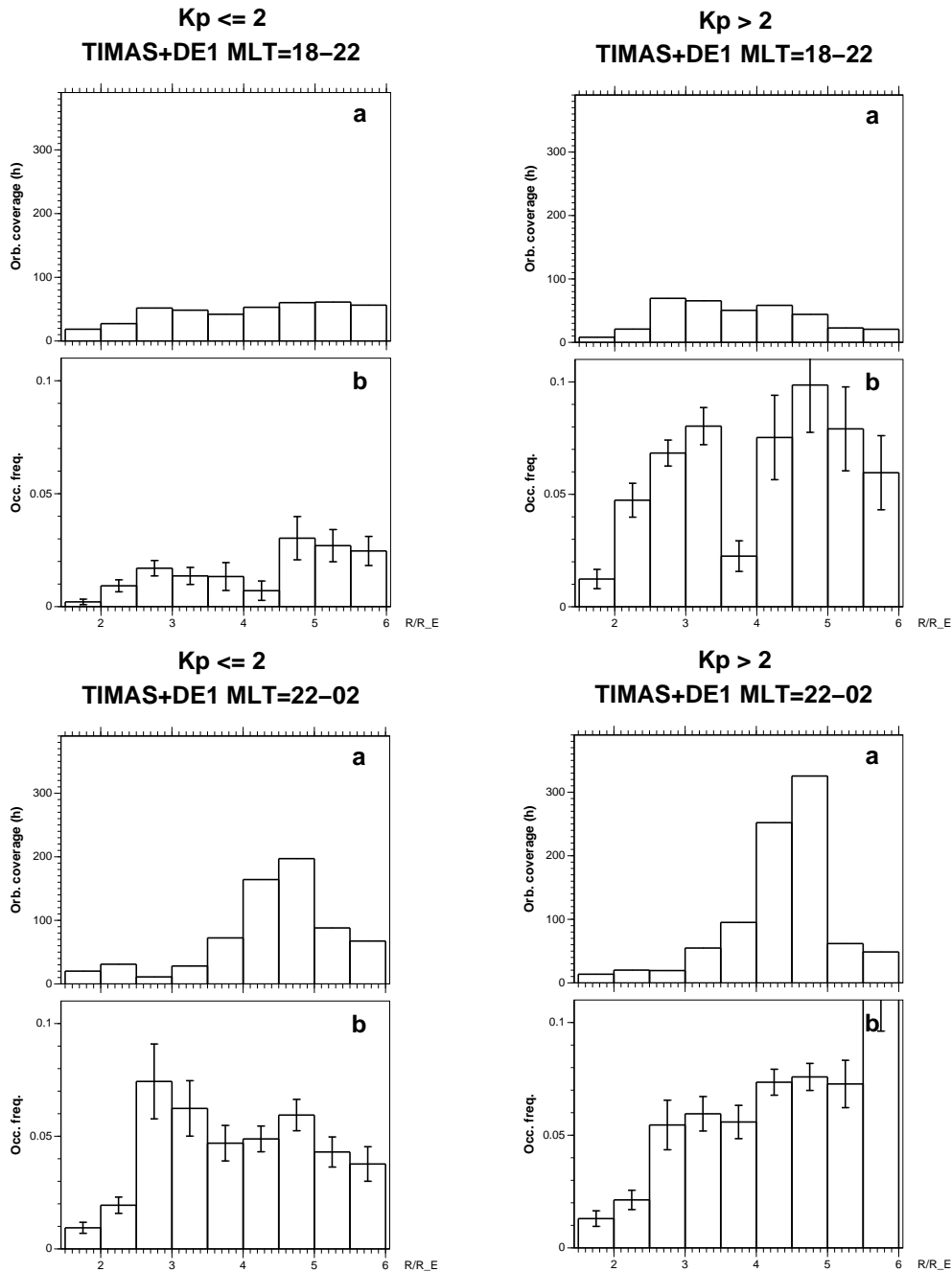
Fig. 3. Ion beam occurrence frequency in 18–22 (top) and 22–02 (bottom) MLT range from combined Polar/TIMAS and DE-1/EICS data when the ionospheric footpoint is in darkness: **(a)** orbital coverage in hours in each bin, **(b)** occurrence frequency of ion beams with energy more than 0.5 keV. Left plots are for $K_p \leq 2$ and right plots for $K_p > 2$.

the closed potential structures (Olsson et al., 2004). In Sect. 4 we will try to reproduce these statistics above 4 R_E by calculating how an Alfvén wave interacts with electrons at different altitudes.

In Fig. 1 we show the occurrence frequency for auroral density cavities. The top panel is the orbital coverage in hours while the remaining panels give the occurrence frequency for spacecraft potential thresholds −11 V, −18 V and −25 V, corresponding roughly to density cavity thresholds of 0.3 cm^{-3}, 0.1 cm^{-3} and 0.06 cm^{-3}, respectively (Scudder et al., 2000). A peak in occurrence frequency around 4–5 R_E is seen in the right panels, i.e. under disturbed conditions. The peak becomes clearer when the absolute value of the spacecraft potential increases. In both quiet and disturbed conditions another peak at 2–3 R_E radial distance is seen, corresponding to auroral cavities (Janhunen et al., 2002).

Error bars are shown in Figs. 1–3 whenever they are not negligibly small. The details of the error bar calculation can be found in Janhunen et al. (2002) for Fig. 1, Janhunen et al. (2004a) for Fig. 2 and Janhunen et al. (2003) for Fig. 3. In short, the error bars are $1/\sqrt{N}$ standard deviations, where N is the number of orbital crossings contributing to the bin.

Figure 2 is for the potential minima. We show the orbital coverage in panel (a). The occurrence frequency of the effective ionospheric electric field E_i (defined as the depth of the potential minimum divided by the half-width of its map in the ionosphere) being larger than $100\,\mathrm{mV/m}$ is shown in panel (b). The occurrence frequency with threshold $500\,\mathrm{mV/m}$ is shown in panel (c). The frequency of E_i has a secondary peak at around 4–$5\,R_E$ during disturbed conditions (panels b and c). The primary occurrence frequency peak seen between 1.5 and $2.5\,R_E$ in Fig. 2 is due to the electrostatic shocks in the classical auroral acceleration region which is not the subject of this paper but which has been extensively studied earlier (Janhunen et al., 2004a).

The occurrence frequency of ion beams from combined Polar/TIMAS and DE-1/EICS data is shown in Fig. 3 (Janhunen et al., 2003). The top sub-figures show results for 18–22 MLT and the bottom sub-figures for 22–02 MLT. Panel (a) shows the orbital coverage in hours in each bin and panel (b) the occurrence frequency of ion beams with energy more than $0.5\,\mathrm{keV}$. The occurrence frequency for ion beams increase around 4–$5\,R_E$ during disturbed conditions (right plots).

In summary, during disturbed conditions, density cavities and potential minima have a peak at 4–$5\,R_E$ radial distance in both evening and midnight MLT sectors (in Figs. 1 and 2, the 18–22 and 22–02 MLT sectors are put together to save journal space). For ion beams (Fig. 3) there is a local peak in ion beam occurrence frequency at 4.5–$5\,R_E$ in the 18–22 MLT sector. In the midnight sector (Fig. 3, bottom sub-figures) the peak is weaker. Thus, an island of cavities occurs in 4–$5\,R_E$, associated with enhanced electric fields. Upgoing ion beams clearly react to the presence of the island in the evening sector, but not significantly in the midnight sector. Since ion beam energisation depends both on static potential structure acceleration, as well as perpendicular wave heating (Janhunen et al., 2003), the exact way how ion beams interact with the cavities and their static and/or dynamic electric fields remains unclear. The main point is to note that in total, three types of independent statistical measurements show that the region 4–$5\,R_E$ radial distance differs from its neighbourhood. Since particles move freely along the magnetic field, some process must consistently act at this altitude to maintain plasma properties that differ from other nearby altitudes. Whether the process is continuous or sporadic, the statistical results do not directly tell, but since the phenomenon occurs only during disturbed conditions, a sporadic process might be expected. Below we will study the possibility of transient Alfvén waves interacting with the plasma.
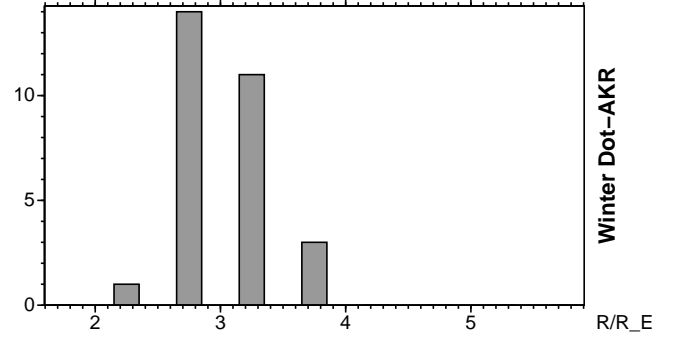

Fig. 4. Altitude-binned histogram of dot-AKR emission radial distance during winter months (November–February) 1996–1997 obtained from Polar PWI instrument. The ordinate is the number of events. Adapted from panel (b) of Fig. 5 of Olsson et al. (2004).

3 Theory

The equations of inertial and kinetic Alfvén waves propagating in a homogeneous plasma have been derived by many authors; see, e.g. Lysak and Lotko (1996). The formulas needed here are conveniently available as Eqs. (2)–(4) of Stasiewicz et al. (2000a). Their region of validity is more fully discussed by Stasiewicz et al. (2000b), pp. 426–438: the frequency ω must be low, i.e. clearly smaller than the ion gyrofrequency ($\omega \ll \Omega_i = eB/m_i$) and the electrons must be cold in the sense that $\xi \equiv \omega/(k_\parallel v_e)$ is larger than unity, so that the derivative of the plasma dispersion function $Z'(\xi) = 1/\xi^2 + (3/2)/\xi^4 + ...$ can be approximated by the first term. Here, v_e is electron thermal velocity. In the numerical examples to follow, the error introduced by using these approximations is ~10% or less in the physically interesting regions.

The ratio of parallel and perpendicular electric fields is

$$\frac{E_\parallel}{E_\perp} = \frac{k_\parallel k_\perp \lambda_e^2}{1 + k_\perp^2 \lambda_e^2}, \tag{1}$$

where $\lambda_e = c/\omega_{pe}$ is the electron inertial length, $\omega_{pe} = \sqrt{ne^2/(\epsilon_0 m_e)}$ is the electron plasma frequency and $k_\perp$ and $k_\parallel$ are the perpendicular and parallel wave number, respectively. Otherwise, the notation is standard: n is the plasma number density, m_e and m_i the electron and ion mass, e the absolute value of the electron charge, c the speed of light and ϵ_0 the vacuum permittivity.

The dispersion relation is

$$\omega = k_\parallel v_A \sqrt{\frac{1 + k_\perp^2 \rho_i^2}{1 + k_\perp^2 \lambda_e^2}}, \tag{2}$$

where $v_A = B/\sqrt{\mu_0 m_i n}$ is the MHD Alfvén speed, μ_0 the vacuum permeability, B the magnetic field strength, $\rho_i = m_i v_s/(eB)$ the ion acoustic gyroradius and $v_s = \sqrt{k_B T_e/m_i}$ the ion acoustic speed. Finally, the E/B ratio of the wave fields is given by

$$\frac{E_\perp}{B_\perp} = v_A \sqrt{(1 + k_\perp^2 \lambda_e^2)(1 + k_\perp^2 \rho_i^2)}. \tag{3}$$

Usually the oblique Alfvén waves obey the flux tube scaling well, i.e. $k_\perp$ scales as $B^{1/2}$ with respect to altitude. At high altitude, an incoming Alfvén wave is more easily kinetic (term $k_\perp \rho_i$ important) than inertial (term $k_\perp \lambda_e$), because the ion acoustic gyroradius ρ_i scales as B^{-1} while λ_e depends only on the density. Notice that the parallel electric field depends only on the inertial character of the wave, not on its kinetic character, while the dispersion relation depends on both.

To close the system of equations we assume that the wave carries all of its original Poynting flux to the ionosphere, without dissipating or reflecting any. Mathematically, this amounts to requiring that $E_\perp B_\perp$ scales as B.

In the following two subsections we apply Eqs. (1)–(3) to study the Alfvén wave acceleration of electrons at the high and low altitude regions at 4–5 R_E (ARS) and 2–3 R_E (pre-existing cavity) radial distance, respectively. For high altitude, Alfvén parallel wavelength is assumed "small" (we apply the usual equations valid for Alfvén waves in homogeneous plasma). For low altitude, the parallel wavelength is large compared to the cavity size and we use a different approach which is explained in Sect. 3.2 below.

3.1 Alfvén resonosphere (ARS) electron acceleration at 4–5 R_E

When an Alfvén wave moves downward towards increasing v_A, its frequency ω stays constant, so Eq. (2) dictates that its parallel wavelength $\lambda_\parallel = 2\pi/k_\parallel$ increases. Thus, for most Alfvén waves, at a high enough altitude $\lambda_\parallel$ is small compared to the scale sizes of the system ($\sim 1\ R_E$) and the equations of homogeneous plasma listed above are valid (the geometrical optics approximation).

Consider trapping of electrons by downgoing Alfvén waves which accelerate downward because $v_{\rm ph}$ increases downward. The aim is to calculate the power density of the process. The resonant electron kinetic energy is

$$W_{\rm res} = (1/2)m_e v_{\rm ph}^2. \tag{4}$$

An electron can only be trapped by the wave if the wave electric field causes an acceleration to the electron which is at least the same as the acceleration a of the wave itself as it moves towards increasing phase velocity regions:

$$\frac{eE_\parallel}{m_e} > a = \frac{dv_{\rm ph}}{dt} = \frac{ds}{dt}\frac{dv_{\rm ph}}{ds} = v_{\rm ph}\frac{dv_{\rm ph}}{ds} = \frac{d}{ds}\left(\frac{v_{\rm ph}^2}{2}\right), \tag{5}$$

where s is a coordinate along the field line. i.e. we obtain a threshold condition for the parallel field to trap the electrons,

$$E_\parallel > \frac{1}{e}\frac{dW_{\rm res}}{ds}. \tag{6}$$

On the other hand, $E_\parallel$ also determines the width of a window in velocity space of trapped electrons so that the window half-width is

$$\Delta v = \sqrt{2e\Delta V_{\rm res}/m_e}, \tag{7}$$

where $\Delta V_{\rm res} = E_\parallel^{\rm eff}(\lambda_\parallel/2)$ is the wave potential. Here

$$E_\parallel^{\rm eff} = \max(0, E_\parallel - \frac{1}{e}\frac{dW_{\rm res}}{ds}). \tag{8}$$

If inequality (Eq. 6) is not satisfied, the window width in velocity space is zero and no electrons are trapped with the wave. When $E_\parallel$ exceeds the threshold (Eq. 6) the window of trapped electrons has a finite width.

For the kinetic energy $W_{\rm kin}$ of an electron trapped by the wave one easily obtains

$$\frac{dW_{\rm kin}}{dt} = v\frac{dW_{\rm res}}{ds}. \tag{9}$$

Consequently, if $g(v)$ is the electron distribution function normalised so that when integrated over v it gives the density, the power density u of the process where the waves are energising the electrons is

$$u = \int_{\max(v_{\rm ph}-\Delta v, 0)}^{v_{\rm ph}+\Delta v} dv\, g(v) v\frac{dW_{\rm res}}{ds}. \tag{10}$$

3.2 Electron acceleration in deep and small low-altitude cavity

At low altitude (2–3 R_E radial distance), the Alfvén speed is typically so high that the parallel wavelength is several R_E. There is often a density cavity at this altitude associated with stable auroral arcs (Fig. 1) whose parallel extent, if estimated from the frequency spread of the dot-AKR emission, is not larger than 1 R_E (Olsson et al., 2004). Therefore, let us assume that an Alfvén wave interacts with a density cavity whose parallel extent is small compared with the parallel wavelength. The goal is to estimate the energy and energy flux to which electrons inside the cavity are accelerated. The Alfvén wave carries a magnetic field $B_\perp$. We make the assumption that $B_\perp$ is undisturbed by the presence of the cavity, i.e. has the same value inside and outside the cavity. Writing Ampere's law inside the cavity we obtain

$$\mu_0 e n v_e = k_\perp B_\perp, \tag{11}$$

where n is the cavity density and $B_\perp$ is the same inside and outside the cavity. The physics of Eq. (11) is that electrons inside the cavity must be accelerated in order to carry the field-aligned current (FAC) of the wave. Using Eq. (3), we can express $B_\perp$ outside the cavity:

$$B_\perp = \frac{E_\perp^0}{v_{A0}\sqrt{1 + k_\perp^2 \lambda_{e0}^2}}, \tag{12}$$

where the index 0 refers to quantities evaluated outside the cavity. For simplicity, we assumed $\rho_i = 0$ which should be nearly always a good assumption at low altitude. To obtain the velocity to which the electrons inside the cavity are accelerated, we solve v_e from Eq. (11) and substitute $B_\perp$ from Eq. (12). We obtain

$$v_e = \frac{n_0}{n}\frac{E_\perp^0}{B}\sqrt{\frac{m_i}{m_e}}\frac{k_\perp \lambda_{e0}}{\sqrt{1 + k_\perp^2 \lambda_{e0}^2}}. \tag{13}$$
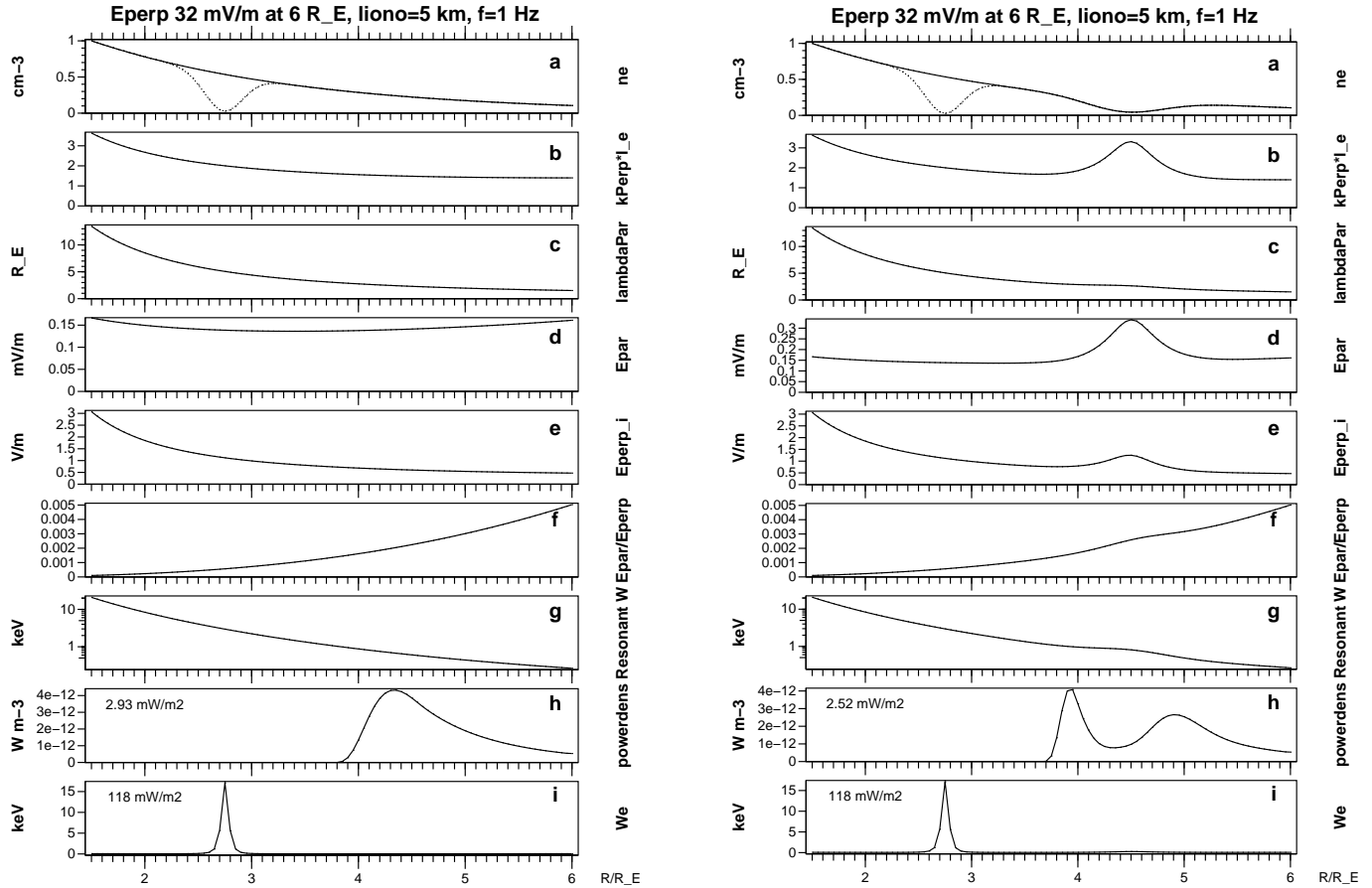
Fig. 5. Panels from top to bottom: electron density profile with rapidly varying "cavity" density profile shown as dotted (**a**), the dimensionless parameter $k_\perp \lambda_e$ (**b**), parallel wavelength (**c**), wave parallel electric field amplitude (**d**), wave perpendicular field mapped to ionosphere with flux tube scaling (**e**), ratio of parallel and perpendicular wave electric fields (**f**), energy of parallel electron that moves with the parallel phase velocity of the wave (**g**), power density of resonant energisation with radially integrated and mapped-to-ionosphere value shown textually (**h**), energy to which electrons must be accelerated to carry the parallel current of the wave with mapped-to-ionosphere energy flux value corresponding to the maximum shown textually (**i**). Left sub-figure is without and right sub-figure with assumed ARS cavity (notice difference in panels (a). Only panel (i) relates to the low-altitude cavity, the other panels have been computed under the assumption of a small wavelength which is not valid in the low-altitude cavity.

Because of the factor n_0/n (density outside the cavity versus density inside the cavity), large electron acceleration may occur in the deepest point of the cavity, if the Alfvén wave is sufficiently intense (depends on $E_\perp^0$).

4 Numerical calculation of Alfvén electron acceleration

We now use the formulas given in Sect. 3 to obtain a quantitative estimate of various parameters associated with Alfvén wave electron acceleration. We assume a magnetic field B that scales as R^{-3}, where R is the radial distance and an altitude-dependent plasma density n. The results of a particular calculation, assuming an incoming Alfvén wave whose perpendicular wavelength is 5 km when mapped to the ionosphere, frequency $f=\omega/(2\pi)=1$ Hz and electric amplitude $E_\perp=32$ mV/m at $R=6\,R_E$, are shown in Fig. 5. The left sub-figure is for the initial phase of ARS electron acceleration,

where the ARS does not yet contain a cavity. The right sub-figure describes the situation some time later (some tens of seconds or some minutes) when a cavity at ARS has formed. Panels (a)–(h) are for ARS and use the formulas given in Sect. 3.1 and panel (i) for a low-altitude cavity using formulas in Sect. 3.2 (panel (i) is similar in both sub-figures). We first give a description for the left sub-figure only, i.e. for the case without ARS cavity, and note the differences caused by the ARS cavity further below.

Panel (a) shows the assumed density profile as a function of R as solid line. (The dotted line is a low-altitude cavity model which is used in panel (i).) Panel (b) is the dimensionless parameter $k_\perp \lambda_e$ corresponding to the density n of panel (a). The wave number $k_\perp$ increases downward as $B^{1/2}$ or $R^{3/2}$, and λ_e decreases downward as $n^{-1/2}$, so $k_\perp \lambda_e$ moderately increases downward. Panel (c) is the parallel wavelength $\lambda_\parallel = 2\pi/k_\parallel$ solved from Eq. (2). Notice that
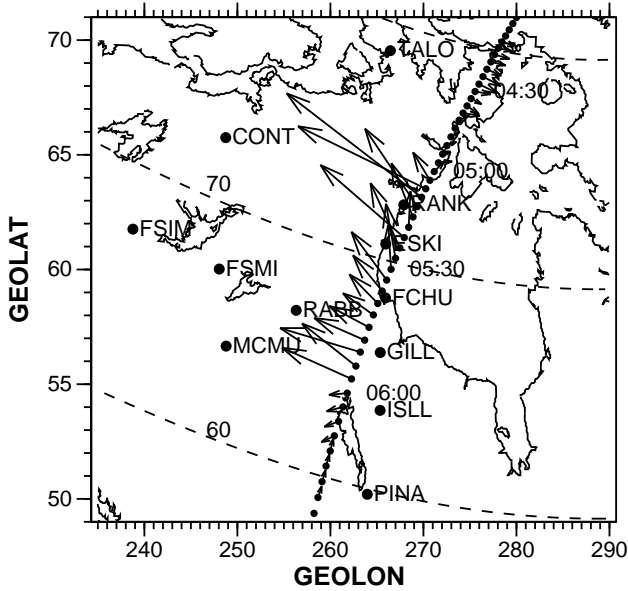
CANOPUS 19970425

Fig. 6. Polar footpoint trajectory over CANOPUS magnetometer network for 25 April 1997, 4:00–6:30 UT. Equivalent current vectors of the magnetometer nearest to the footpoint is shown by arrows (arbitrary scale). Circles of constant invariant latitude are shown as dashed lines. UT times are shown on the right side of the trajectory.

$\lambda_\parallel$ increases rapidly downward and is very long at low altitudes. Panel (d) shows the wave parallel electric field $E_\parallel$, panel (e) the perpendicular field mapped to ionosphere using flux tube scaling and panel (f) the $E_\parallel/E_\perp$ ratio. The ratio $E_\parallel/E_\perp$ decreases rapidly downward mainly because it is proportional to $k_\parallel$ (Eq. 1). However, because $E_\perp$ scales similarly to $k_\perp$, i.e. as $B^{1/2}$, the net result for $E_\parallel$ is a modest downward decrease. Panel (g) is the resonant electron energy W_{res} (Eq. 4); it rapidly increases downward because it is approximately proportional to B^2 or R^{-6} (notice the logarithmic scale). Panel (h) is the power density u (Eq. 10), calculated assuming 100 eV electron temperature. The radial integral of the power density weighted by the flux tube factor B_i/B (B_i is the ionospheric magnetic field 50 000 nT, $B_i=B(R=1\ R_E)$) is the power flux in the ionosphere, whose value in this case is 2.93 mW m^{-2}. If deposited as electron precipitation in the ionosphere (which does not happen), this power flux would be enough for a weak, marginally visible auroral arc.

Panel (i) of Fig. 5 corresponds to the situation described in Sect. 3.2 above where an Alfvén wave accelerates electrons inside a cavity, and it shows the energy $W_e=(1/2)m_e v_e^2$ corresponding to the accelerated electron velocity v_e given in Eq. (13). At a moment when the wave's field-aligned current is upward, all electrons inside the cavity are accelerated downward. Assuming that the formed downward beam is so narrow that all the electrons precipitate, they carry to the ionosphere an energy flux ϵ (W m^{-2}) which is given by
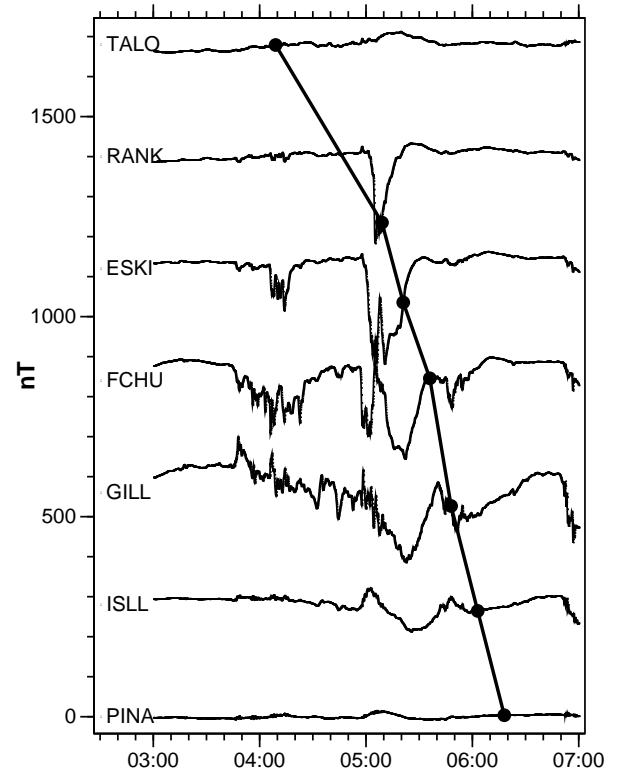
CANOPUS 19970425

Fig. 7. Stacked plot of CANOPUS magnetogram X components (northward components) for 25 April 1997. Between 5–6 UT a negative bay of a substorm is most strongly seen in Rankin Inlet (RANK), Eskimo Point (ESKI), Fort Churchill (FCHU) and Gillam (GILL). The times when Polar intersects the ILAT circle of each magnetometer are shown as dots and connected by a line.

$$\epsilon = n_{\mathrm{cav}} v_e W_e \frac{B_i}{B}, \tag{14}$$

where n_{cav} is the minimum density inside the cavity and v_e and W_e are, respectively, the electron velocity and energy corresponding to that density and B is the magnetic field, at the minimum density location. In this case $\epsilon=118$ mW m^{-2} and the maximum energy to which the electrons are accelerated is $\sim$15 keV. This would be enough to cause a bright substorm onset auroral display in the ionosphere.

Comparing the left (no ARS cavity) and right (with ARS cavity developed) sub-figures of Fig. 5, the presence of an ARS cavity affects the ARS electron acceleration in the following ways. The wave becomes more inertial at ARS ($k_\perp \lambda_e$ makes a hump there, panel (b). Also $E_\parallel$ (panel (d)) and $E_{\perp i}$ (panel (e)) are enhanced there, which is in agreement with the enhanced electric fields at the high altitude island (Fig. 2). Since the resonant energy profile (panel (g)) is less monotonic than without the ARS cavity (left sub-figure), the trapping of electrons is disturbed, resulting in a more complex power density profile (panel (h)).

5 Events for 2–3 and 4–5 R_E

5.1 Electron acceleration in ARS

In this subsection we describe an event where Polar resides at 4–5 R_E radial distance with its footpoint mapping in a modest ($\sim$250 nT) substorm which occurred on 25 April 1997 over the Canadian CANOPUS ground-based magnetometer network. Figure 6 shows the footpoint trajectory of Polar over the CANOPUS magnetometer network. The seven stations Taloyoak (TALO), Rankin Inlet (RANK), Eskimo Point (ESKI), Fort Churchill (FCHU), Gillam (GILL), Island Lake (ISLL) and Pinawa (PINA), form the main chain running from north to south. In this event the main chain coincides rather well with the Polar trajectory. Other CANOPUS stations on the eastern side of the chain (Contwoyto Lake CONT, Fort Simpson FSIM, Fort Smith FSMI, Rabbit Lake RABB and Fort McMurray MCMU) are also shown in Fig. 6. The equivalent current vectors corresponding to the main chain station which is most nearby the Polar footpoint are shown as arrows in arbitrary scale. The equivalent current vectors are determined by subtracting a baseline which is the average field measured between 2:00 and 3:00 UT during the same day, 25 April 1997. Approximate times of Polar are displayed in Fig. 6 on the right side of the footpoint trajectory.

Figure 7 shows the geographic north component (X component) of the magnetograms for the main chain stations after the removal of a baseline. For each station, the time when Polar intersects the ILAT circle of the station is found and marked by the abscissa of a dot. The ordinate of the dot is taken to be the measured magnetic field so that the dots lie on the magnetogram curves. The dots are connected by lines to show the temporal order. The first negative bay is seen at Fort Churchill (FCHU, 69.5 ILAT) at 04:58, from which it spreads northward to Eskimo Point (ESKI, 71.8 ILAT) and Rankin Inlet (RANK, 73.5 ILAT) in less than 10 min. Polar enters the substorm when its footpoint approaches Rankin Inlet from the north, which is evidenced by a few long equivalent current vectors in Fig. 6 near RANK. The perturbations never reach Taloyoak (TALO, 79.5 ILAT) in the north and Pinawa (PINA, 61 ILAT) in the south. Data from stations east of the main chain do not show strong perturbations, so that the substorm is confined near the main chain. In this study we are not interested in a detailed correspondence between ground-based and satellite observations, but the purpose of Figs. 6 and 7 is to document that a substorm is going on in the Polar footpoint area when Polar crosses the auroral oval.

Figure 8 shows Polar spacecraft potential and electron data during the event. Panel (a) is the spacecraft potential from the Electric Fields Investigation (EFI) instrument (Harvey et al., 1995). Polar is in the polar cap until 05:22, in a "quiet" auroral oval 05:22–05:42 and in active auroral field lines after 05:42. After 06:00 Polar moves to subauroral latitudes. Panels (b)–(d) show the downward, perpendicular and upward electron differential energy flux F, respectively, from the HYDRA electron detector (Scudder et al., 1995). Panel

(e) is the ratio $F_\parallel/F_\perp$, where $F_\parallel = (1/2)(F_{\mathrm{upward}} + F_{\mathrm{downward}})$ is the field-aligned and $F_\perp$ the perpendicular differential energy flux. Red colour in panel (e) signifies an electron distribution where the parallel flux is enhanced with respect to the perpendicular flux at the same energy. For a discussion of ways to quantify these kinds of electron anisotropies and their statistical properties in the auroral region, see Janhunen et al. (2004b). The features seen in panels (b)–(e) are typical of active auroral field lines: there is an enhanced, almost isotropic hot electron population at several keV energy, together with a strongly anisotropic $T_\parallel > T_\perp$ type middle-energy (100–1000 eV) distribution.

Figure 9 shows the Polar HYDRA electron distribution function at one time (05:42:40) which is rather representative of the interval where the Alfvén waves are seen. There is a strong $T_\parallel > T_\perp$ type anisotropy below 1 keV, while above 1 keV the distribution is isotropic. As mentioned above, this type of middle-energy electron anisotropies, together with isotropic high-energy distributions, are common in auroral field lines. In this event, because there is simultaneous Alfvén wave activity, we suggest that the middle-energy anisotropy is at least partly due to Alfvén waves being in Landau resonance with the electrons (Wygant et al., 2002). This is not the only possible interpretation. For example, we have suggested before that ion Bernstein waves cause somewhat similar anisotropies in auroral field lines during more quiet times at many altitudes (Olsson and Janhunen, 2004). Alfvén waves are relatively rare, but electrostatic waves and anisotropies are both common in this region. However, we still think that the Alfvén acceleration idea is sensible in this event, since the anisotropy seen is stronger than what is typically seen during quiet times.

Figure 10 shows data from the Polar electric and magnetic field instruments. Panel (a) is the spectrogram of the spin-plane electric field below 10 Hz, taken from the full time resolution (20 samples per second) data of EFI using the Hanning window in 60-s boxes. The quantity shown is the square root of the total spectral power in all of the Cartesian GSE components of the field. Panel (b) is the corresponding magnetic field spectrogram from the Magnetic Field Experiments (MFE) (Russell et al., 1995) below 4 Hz, again using the full resolution data (8 samples per second). Panel (c) is the ratio of panels (a) and (b), i.e. the E/B ratio of the wave field. One clearly sees from Fig. 10 that intense wave activity occurs between 05:40 and 05:50 and that the E/B ratio of the waves is less than 10^8 m/s, even less than 10^7 m/s for the most intense waves below 0.1 Hz. An estimated MHD Alfvén speed is $\sim 2 \times 10^7$ m/s. The E/B ratio and the spectral signatures suggest that the waves are Alfvénic. The wave activity occurs simultaneously when HYDRA detects enhanced hot isotropic electrons, together with the middle-energy anisotropies (see previous paragraph). The magnetic component of the waves is small in the 2–4 Hz range (above 4 Hz we have all reason to assume this to be the case as well, although we have no data there), which is consistent with the Alfvénic interpretation: the shear Alfvén wave dispersion surface exists only below the ion gyrofrequency, which is $\sim$7 Hz locally,
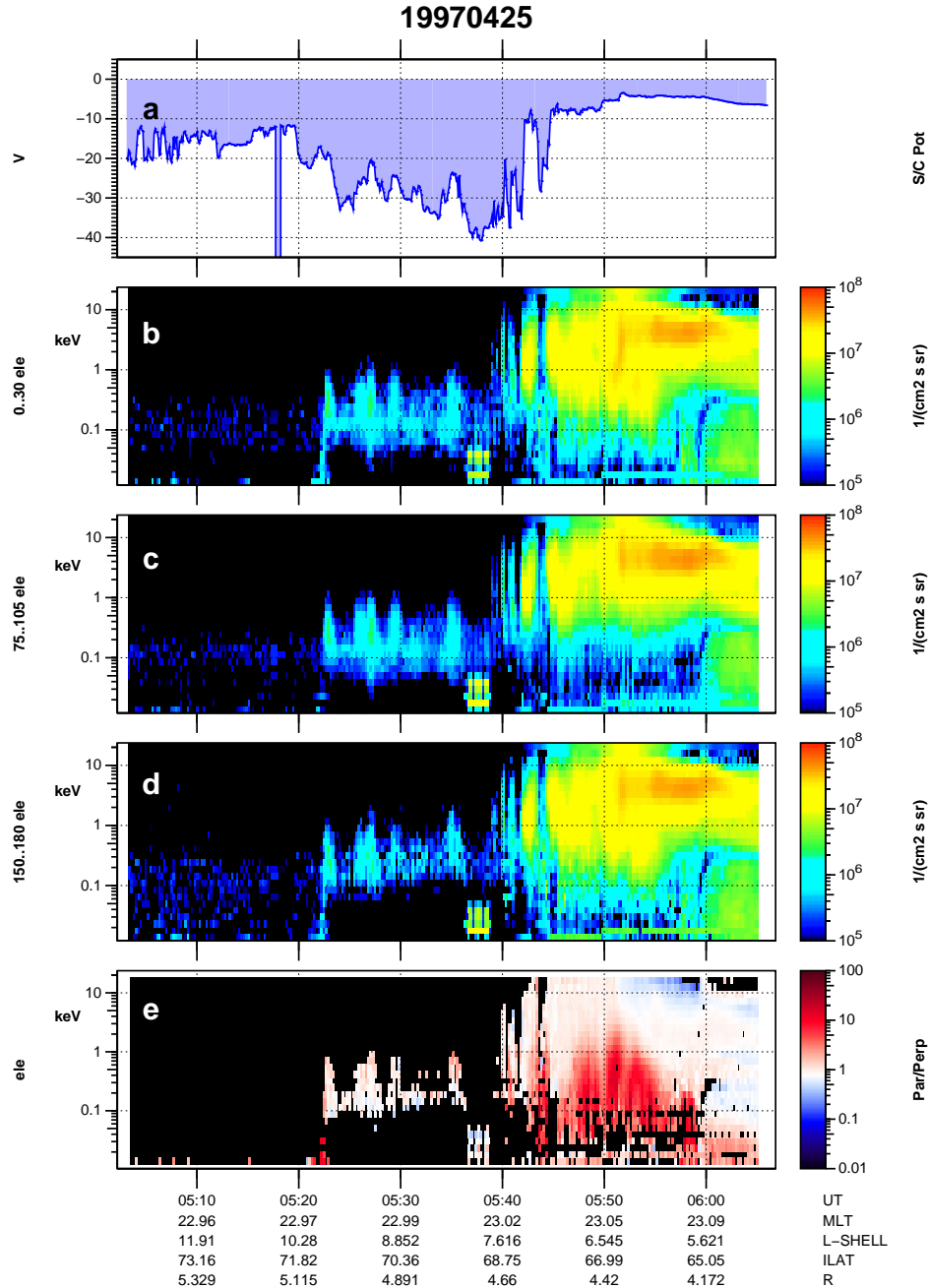
19970425

Fig. 8. Polar data for 25 April 1997, 5:03–6:07 UT. EFI spacecraft potential **(a)**, HYDRA downgoing **(b)**, perpendicular **(c)** and upgoing **(d)** electron differential energy flux, and ratio between parallel and perpendicular fluxes **(e)**. The satellite moves from the polar cap into the auroral zone 5:42 UT.

but smaller deep in the magnetotail where the source region for the substorm-related Alfvén waves probably resides. Although the exact location of the source region is not known, typical fields in the magnetotail are usually not larger than 100 nT, so seeing Alfvén-waves at higher than ∼2 Hz frequency would indicate either a low-altitude source or significant nonlinear cascading in frequency space; there is no evidence for such processes in this event.

5.2 Electron acceleration in auroral cavity (2–3 R_E)

We now study Interball data in an event where the satellite was at 3.5 R_E radial distance during a substorm on 11 December 1998, 13:00–13:30 UT (Fig. 11). We show the E and B spectrograms from the low-frequency wave instrument IESP on board Interball Auroral Probe (Perraut et al., 1998) in panels (a) and (b), respectively. At times marked with small black arrows in Fig. 11 there is an artificial signal from the NVKONCH instrument which shows
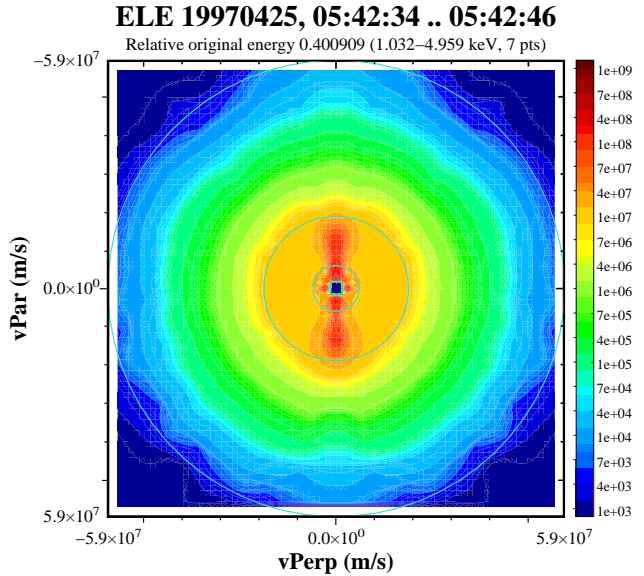
Fig. 9. HYDRA electron distribution function taken at 05:42:40 (central time) and integrated over 12 s. Blue circles are drawn at velocities corresponding to energy 10 keV, 1 keV, 100 eV and 10 eV (the innermost one is quite small, the inside of which is shown as dark blue). Above 1 keV the distribution is isotropic but between 100–1000 eV (and partly below 100 eV also) it is strongly anisotropic.

Fig. 10. E, B, and E/B ratio from Polar EFI and MFE instruments. EFI spin plane electric field spectrogram **(a)**, MFE spectrogram **(b)**, ratio of panels (a) and (b) **(c)**. Estimated MHD Alfvén speed is $\sim 2 \times 10^7$ m/s.

up in the IESP panels. Datapoints of panel (b) (wave magnetic spectrogram), where the magnetic spectral density is below 3×10^{-11} T Hz$^{-1/2}$, are shown as white in panel (c) (the E/B ratio). Panel (c) shows the E/B ratio, where green corresponds to Alfvén waves and red to electrostatic waves (13:18–13:20 UT). Panel (d) shows the high-frequency spectrogram from the POLRAD instrument (Hanasz et al., 1998), but presented so that the vertical axis is the radial distance R rather than the frequency f. The assumptions made in connection f and R are that the f corresponds to the electron gyrofrequency in the generation region, $f = (eB/m_e)/(2\pi)$ and that the magnetic field at the generation region is given by $B = B_i (R_E/R)^3$, where $B_i = 50\,000$ nT is the ionospheric magnetic field. Normal AKR is seen in panel (d) until 13:25, generated below the $2\,R_E$ radial distance. A clear dot-AKR emission (Hanasz et al., 1998; de Feraudy et al., 2001; Olsson et al., 2004) is seen at $\sim$13:20 UT at $\sim 3\,R_E$. Our interpretation is that the dot-AKR emission is a result of localised electron acceleration at $\sim 3\,R_E$ radial distance which is due to the intense substorm-related Alfvén waves. We suggest to explain the rather narrow altitude range of the dot-AKR emission, which is clearly above the main acceleration region generating normal AKR, by the presence of a small auroral density cavity. Although there is no independent confirmation of the vertical size of the cavity, the statistical fact that the dot-AKR originates near the same altitude where the deepest cavities are statistically seen (Fig. 4, for more details, see Olsson et al., 2004) makes this interpretation plau-
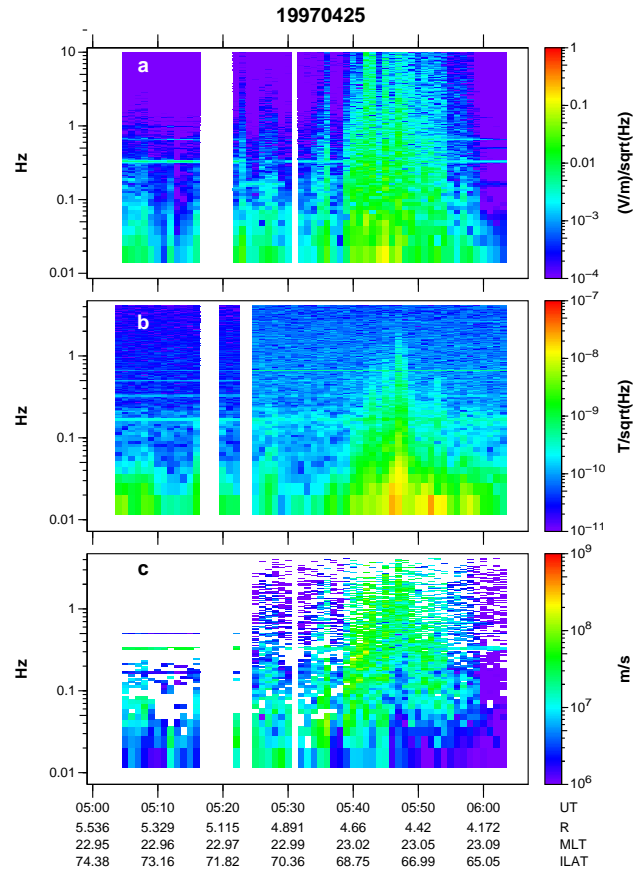
sible: the dot-AKR emission and the presence of the cavity are probably related, and the cavity size is the most natural defining factor for the frequency spread and thus the altitude spread of the electron acceleration which causes the dot-AKR emission.

6 Discussion

The purpose of this paper was to develop the idea of the Alfvén Resonosphere (ARS), to describe the high-altitude 4–5 R_E "island" seen in many data sets during disturbed conditions, and compare and contrast it with the Alfvénic model for dot-AKR formation at 2–3 R_E during substorm onsets.

We introduced the concept of ARS which means the quasi-spherical layer at $\sim$4–5 R_E where the local (MHD) Alfvén speed is near the local electron thermal speed. In ARS, electrons can therefore be accelerated by a Landau resonance of an Alfvén wave. The exact location of ARS, of course, depends on the plasma density and electron temperature, but because $v_A \sim B \sim 1/R^3$ depends strongly on R and more weakly on the density, ARS is rather well-defined and not a very thick region. The main observational support
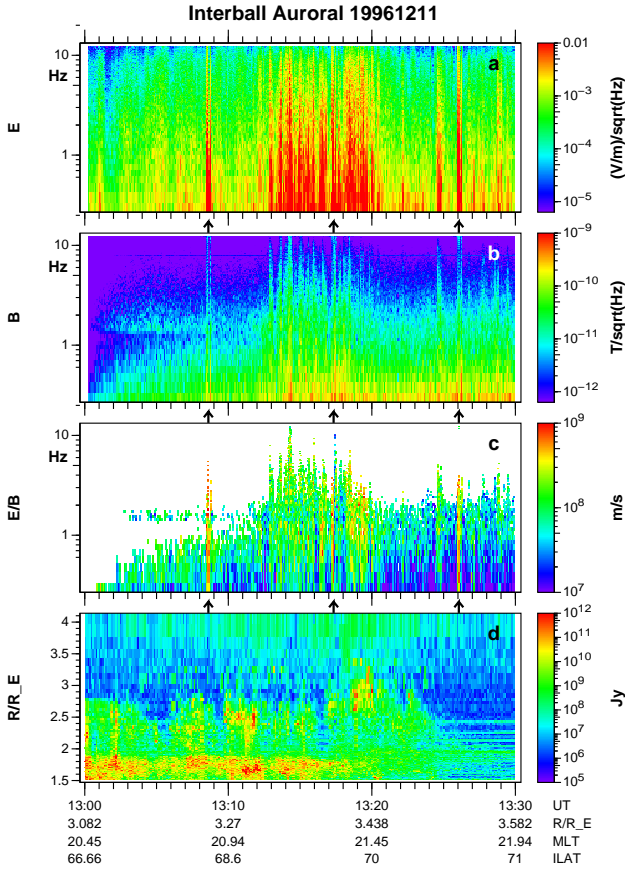
Fig. 11. Dot AKR example event 11 December 1996 with IESP and POLRAD data, showing **(a)** electric IESP wave amplitude, **(b)** magnetic IESP wave power, **(c)** the E/B ratio from IESP and **(d)** POLRAD AKR data. The vertical axis in panels (a)–(c) is Hz. The intensity in panel **(d)** is in Jansky (1 Jy = 10^{-26} W m^{-2} Hz^{-1}). The vertical axis in panel (d) is the radial distance corresponding to the AKR frequency, assuming the frequency corresponds to local electron gyrofrequency. The dot AKR seen at 13:18–13:20 at $\sim$3 R_E radial distance (45–70 kHz) occurs simultaneously with electromagnetic low frequency wave activity. Dots at 13:01–13:02, 13:07–13:08 and 13:09–13:11 are not associated with low frequency waves.

for the relevance of ARS is that at 4–5 R_E there is statistically a region of reduced plasma density and enhanced electric fields during disturbed conditions in the midnight and evening MLT sectors. Since Alfvén waves are known to be most intense during substorms and also since substorm activity occurs mainly in the midnight and evening sectors, the idea that the cavity seen at 4–5 R_E is caused by Alfvén wave induced electron acceleration appears to be quite plausible.

In an event where Polar is known from ground-based measurements to be inside a substorm and at 4–5 R_E radial distance (i.e. at ARS), we found that the electron distribution below 1 keV is indeed highly anisotropic, indicating energy-selective parallel electron heating by waves. Simultaneous intense Alfvén waves below 2 Hz were found in Polar electric and magnetic field data. The plasma potential varies between -40 V and -10 V when the Alfvén waves are seen;

-40 V corresponds to a deep cavity of less than $\sim$0.05 cm^{-3} while -10 V corresponds to density $\sim$0.3 cm^{-3}. Notice that since the density cavity cannot develop faster than the ions move, it does not form immediately when the Alfvén activity starts, so a one-to-one correspondence between Alfvén wave activity and cavity depth is not expected to occur.

The theoretical and numerical part showed that modest energy deposition in ARS, corresponding to a few milliwatts per square meter in the ionosphere, is expected to occur when intense (32 mV/m electric amplitude at 6 R_E) Alfvén waves are present. Even though the energy flux is only modest by the auroral ionosphere standard, it is still enough to energise all middle-energy electrons in ARS in $\sim$1 s to $\sim$500 eV, as it should be consistent with our interpretation since the travel time of electrons through ARS is also $\sim$1 s.

For the low-altitude cavity, our calculations predict much larger, up to 118 mW m^{-2}, ionospheric equivalent energy flux and up to 15 keV maximum energy. Even larger values could be obtained by assuming a deeper cavity or higher amplitude Alfvén wave. These values should not be taken as accurate estimates, however, since probably not all the electrons are able to precipitate in the ionosphere and also our model for the cavity is a crude one. Also our initial assumption that the wave carries all Poynting flux to the ionosphere overestimates the wave amplitude at low altitude, since part of the energy is in reality reflected or dissipated. Equations (13) and (14) show that the power flux $\epsilon \sim E_\perp^3/n^2$ and the electron energy is $W_e \sim E_\perp^2/n^2$, where $E_\perp$ is the Alfvén wave amplitude and n the minimum density in the cavity. Thus, electron acceleration in the low-altitude cavity is sensitive to the minimum density and the Alfvén wave amplitude. These properties are in accordance with the observed fact that the dot-AKR emission is rather rare and only associated with substorm onsets. Outside major storms at least, substorm onsets are the events where the brightests and fastest moving (i.e. Alfvénic) auroral phenomena are seen and where electron energies are reported to reach 30 keV (Olsson et al., 1998). Apart from the energy given to dot-AKR, the accelerated electrons could also explain the field-aligned bursts often seen superposed with inverted-V electrons in FAST (Chaston et al., 2002) and sounding rocket data (Tung et al., 2002).

Our electron density statistics (Fig. 1) show that the lowest densities occur between 2.5–3 R_E (9500–13 000 km altitude). This is a higher altitude than where normal AKR is generated: the typical normal AKR frequency of 400 kHz corresponds to only 3300 km altitude. An important parameter that controls AKR emission is the ratio ω_{pe}/Ω_e, where $\omega_{pe} = \sqrt{ne^2/(\epsilon_0 m_e)}$ is the electron plasma frequency and $\Omega_e = eB/m_e$ is the electron gyrofrequency (Wu and Lee, 1979; Hilgers, 1992; Benson, 1995). To enable AKR emission, ω_{pe}/Ω_e must be smaller than approximately 0.1–0.2 (Hilgers, 1992; Benson, 1995). From this it follows that the largest density at each altitude that enables AKR emission scales as R^{-6}, where R is the radial distance. Thus, the fact that deep cavities are rarely seen in our data at very low

altitude (below 2.5 R_E radial distance) is in agreement with the AKR versus density study of Hilgers (1992).

We can also envision three other mechanisms that contribute in the same direction, i.e. that low-altitude deep cavities are rarely seen in the spacecraft potential data. The first mechanism is due to the measurement method: the spacecraft potential depends not only on the density but also to some extent on the electron energies. Specifically, Fig. 2 of Janhunen et al. (2002) shows that a cold plasma with density $0.05\,\mathrm{cm}^{-3}$ corresponds to Polar spacecraft potential of 25 V, but if the plasma has temperature 6 keV, the spacecraft potential is 12 V. Thus our method of building the density statistics may miss those low density regions which contain strong fluxes of high energy electrons (inverted-V electrons). Since the inverted-V electron fluxes are the most intense below the bottom of the acceleration region, this mainly contributes towards missing low-altitude cavities.

The second mechanism is that the strongest electron acceleration events probably correspond to the deepest cavities and the lowest acceleration region bottom altitudes; however, the downward-reaching negative potential fingers causing these events are narrow and probably also short-lived. Thus the events are spatially rare, although they may emit a significant fraction of normal AKR. The third mechanism is related to cavity lifetime effects. After the active processes stop or move elsewhere, the formed cavity fills up in the cold (ambient) ion time scale, starting from its bottom. Typically, the process takes $\sim$10 min (Janhunen and Olsson, 2002). The lower the altitude, the faster the filling up process is because the ions then need to move a shorter distance. Thus, the fraction of "dead" (nonradiating) cavities seen in the density depletion statistics increases with altitude. To summarise, deep low-altitude cavities in the spacecraft potential statistics are rarely seen because (1) although significant contributors to normal AKR, they are spatially rare, (2) to emit normal AKR at low altitude, small plasma density which is not very small is actually required, (3) even when a deep cavity exists at low altitude, it usually contains intense inverted-V electron fluxes which make the plasma look denser than it is in the spacecraft potential sense, (4) when the inverted-V electron activity stops, the low-altitude part of the cavity quickly fills up.

We summarise our scenario by the cartoon diagram shown in Fig. 12. In the initial state (panel (a)), only a low-altitude auroral cavity associated with a stable auroral arc and maintained by, for example, the cooperative model involving ion Bernstein waves exists (Olsson and Janhunen, 2004). In panel (b), substorm onset associated Alfvén waves arrive from the magnetosphere, causing electron acceleration in ARS where $v_A \approx v_e$. At low altitude the wave produces dot-AKR emission when accelerating electrons inside a pre-existing auroral cavity. In panel (c), the Alfvén wave activity has lasted for some time (from some tens of seconds to some minutes) and electron acceleration has caused some ions to leave ARS as well, leading to an ARS cavity. In panel (d) the Alfvén-wave activity has stopped. The ARS cavity refills in the ion time scale so that it continues to exist for some
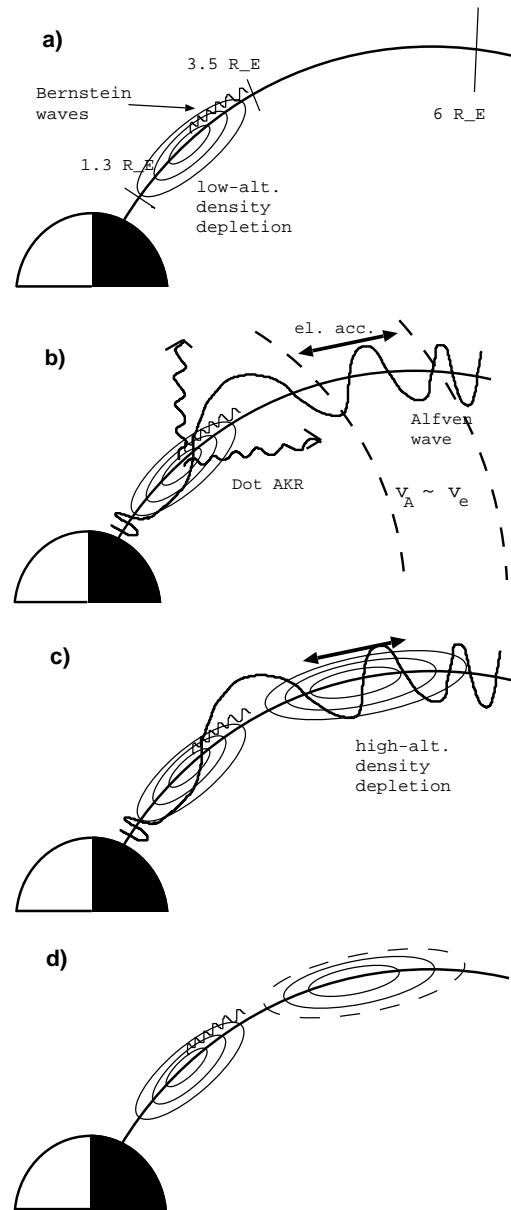

Fig. 12. Our view of processes that Alfvén-wave activity causes on auroral field lines: **(a)** low-altitude auroral cavity associated with stable auroral arc and maintained by, for example, the cooperative model involving ion Bernstein waves (Olsson and Janhunen, 2004), **(b)** at substorm onset, Alfvén waves arrive from the magnetosphere, causing electron acceleration in the Alfvén resonosphere (ARS) where $v_A \approx v_e$ and possibly also dot-AKR emission in the low-altitude cavity (the dot-AKR emission is usually short-lived and probably requires strong transient Alfvén waves), **(c)** if Alfvén wave activity lasts for some time, electron acceleration causes some ions to leave ARS as well, leading to an ARS cavity, **(d)** after the Alfvén-wave activity has stopped, the ARS cavity fills up in the ion time scale, so that it continues to exist for some time (the low-altitude depletion is all the time maintained by other processes which are independent of Alfvénic acvitity). Normal AKR is emitted all the time near the lower boundary of the cavity, although not shown.

time. The low-altitude cavity is all the time maintained by other processes which are independent of Alfvénic acvitity. To prevent the figure from becoming too messy, the normal AKR emitted by the cavity all the time is not shown.

Finally, to put the paper in context, we address the following question: what is the role of transient Alfvén waves in optical auroral phenomena in light of this study? The main transient Alfvénic effects in active aurora are motion and brightenings of auroral forms. These effects are superposed to the stable arc maintaining processes which need not be (and probably are not) Alfvénic. Auroral motion is the optical signature of energy deposited in the ionosphere by Joule heating because the motion is the $E \times B$ drift of the Alfvén wave electric field. Auroral brightenings are probably due to Alfvénic power dissipated to electrons in the acceleration region, producing field-aligned electron fluxes. It was a topic of this paper that in substorm onsets, the Alfvén waves accelerate electrons within pre-existing cavities rapidly enough so that dot-AKR emissions also result. Energetically, the dot-AKR process is probably not important, but it has potential remote sensing diagnostic value as a cavity altitude marker. The ARS electron acceleration is important because it causes large effects, for example, in the form of cavity formation at 4–5 R_E, although ARS is also not very significant energetically: only a small fraction of the incoming Alfvén wave energy goes into electrons in the ARS, the rest propagates to lower altitudes and is dissipated or reflected (Lysak and Song, 2003b). Consideration of Alfvénic electron acceleration below the main acceleration region where the increase in the plasma density reduces the Alfvén speed, bringing it again to Landau resonance with electrons, is outside the scope of this paper.

References

Benson, R. F.: Comment on "The auroral radiating plasma cavities" by Hilgers, A., Geophys. Res. Lett., 22, 3005–3007, 1995.

Chaston, C. C, Bonnell, J. W., Peticolas, L. M., Carlson, C. W., and McFadden, J. P.: Driven Alfvén waves and electron acceleration: a FAST case study, Geophys. Res. Lett., 29, 11, doi:10.1029/2001GL013842, 2002.

de Feraudy, H., Hanasz, J., Schreiber, R., Parks, G., Brittnacher, M., Perraut, S., Sauvaud, J. A., Lefeuvre, F., and Mogilevsky, M.: AKR bursts and substorm field line excitation, Phys. Chem. Earth, 26, 151–159, 2001.

Génot, V., Louarn, P., and Mottez, F.: Electron acceleration by Alfvén waves in density cavities, J. Geophys. Res., 105, 27 611–27 620, 2000.

Haerendel, G.: An Alfvén wave model of auroral arcs, in: High Latitude Space Plasma Physics, edited by Hultqvist, B. and Hagfors, T., Plenum, New York, 515, 1983.

Hasegawa, A.: Particle acceleration by MHD surface wave and formation of aurora, J. Geophys. Res., 81, 5083–5090, 1976.

Hui, C.-H. and Seyler, C. E.: Electron acceleration by Alfvén waves in the magnetosphere, J. Geophys. Res., 97, 3953–3963, 1992.

Hanasz, J., Krawczyk, Z., Mogilevsky, M. M., Schreiber, R., de Feraudy, H., Dudzinski, K., Romantsova, T. V., Nowakiewicz, W., Kraynyuk, A., Barylko, M., Buczkowska, A., Juchniewicz, J., Nazarov, V. N., and Mikhalev, N.: Observations of auroral kilometric radiation on board Interball-2: Polrad experiment, Cosmic Res., 36, Engl. Transl., 575–586, 1998.

Hanasz, J., de Feraudy, H., Schreiber, R., Parks, G., Brittnacher, M., Mogilevsky, M. M., and Romantsova, T. V.: Wideband bursts of auroral kilometric radiation and their associated with UV auroral bulges, J. Geophys. Res., 106, 3859–3871, 2001.

Harvey, P., Mozer, F. S., Pankow, D., Wygant, J., Maynard, N. C., Singer, H., Sullivan, W., Anderson, P. B., Pfaff, R., Aggson, T., Pedersen, A., Fälthammar, C. G., and Tanskanen, P.: The electric field instrument on the Polar satellite, Space Science Reviews, 71, 583–596, 1995.

Hilgers, A.: The auroral radiating plasma cavities, Geophys. Res. Lett., 19, 237–240, 1992.

Janhunen, P., Olsson, A., and Laakso, H.: Altitude dependence of plasma density in the auroral zone, Ann. Geophys., 20, 1743–1750, 2002.

Janhunen, P., Olsson, A., and Peterson, W. K.: The occurrence frequency of upward ion beams in the auroral zone as a function of altitude using Polar/TIMAS and DE-1/EICS data, Ann. Geophys., 21, 2059–2072, 2003.

Janhunen, P. and Olsson, A.: The occurrence frequency of auroral potential structures and electric fields as a function of altitude using Polar/EFI data, Ann. Geophys., in press, 2004a.

Janhunen, P., Olsson, A., and Laakso, H.: Middle-energy electron anisotropies in the auroral region, Ann. Geophys., 22, 1–13, 2004b.

Janhunen, P. and Olsson, A.: A hybrid simulation model for a stable auroral arc, Ann. Geophys., 20, 1603–1616, 2002.

Louarn, P., Wahlund, J.-E., Chust, T., de Féraudy, H., Roux, A., Holback, B., Dovner, P. O., Eriksson, A. I., and Holmgren, G.: Observation of kinetic Alfvén waves by the Freja spacecraft, Geophys. Res. Lett., 21, 1847–1850, 1994.

Lysak, R. L. and Carlson, C. W.: The effect of microscopic turbulence on magnetosphere-ionosphere coupling, Geophys. Res. Lett., 8, 269–272, 1981.

Lysak, R. L. and Lotko, W.: On the kinetic dispersion relation for shear Alfvén waves, J. Geophys. Res., 101, 5085–5094, 1996.

Lysak, R. L. and Song, Y.: Kinetic theory of the Alfvén wave acceleration of auroral electrons, J. Geophys. Res., 108, A4, 8005, doi:10.1029/2002JA009406, 2003a.

Lysak, R. L. and Song, Y.: Nonlocal kinetic theory of Alfvén waves on dipolar field lines, J. Geophys. Res., 108, A8, 1327, doi:10.1029/2003JA009859, 2003b.

Olsson, A., Andersson, L., Eriksson, A. I., Clemmons, J., Erlandsson, R. E., Reeves, G., Hughes, T., and Murphree, J. S.: Freja studies of the current-voltage relation in substorm related events, J. Geophys. Res., 103, 4285–4301, 1998.

Olsson, A. and Janhunen, P.: Some recent developments in understanding auroral electron acceleration processes, IEEE Trans. Plasma Sci., in press, 2004.

Olsson, A., Janhunen, P., Mogilevsky, M., Hanasz, J., Perraut, S., and Menietti, J. D.: Observational study of generation mechanism of substorm-associated low-frequency AKR emissions, Ann. Geophys., in press, 2004.

Perraut, S., Roux, A., Darrouzet, F., de Villedary, C., Mogilevsky, M., and Lefeuvre, F.: ULF wave measurements onboard the Interball auroral probe, Ann. Geophys., 16, 1105–1116, 1998.

Russell, C. T., Snare, R. C., Means, J. D., Pierce, D., Dearborn, D., Larson, M., Barr, G., and Le, G.: The GGS/Polar Magnetic Fields Investigation, Space Sci. Rev., 71, 563–582, 1995.

Samson, J. C., Rankin, R., and Tikhonchuk, V. T.: Optical signatures of auroral arcs produced by field line resonances: comparison with satellite observations and modeling, Ann. Geophys., 21, 933–945, 2003.

Scudder, J. D., Hunsacker, F., Miller, G., Lobell, J., Zawistowski, T., Ogilvie, K., Keller, J., Chornay, D., Herrero, F., Fitzenreiter, F. R., et al.: Hydra – A 3-dimensional electron and ion hot plasma instrument for the Polar spacecraft of the GGS mission, Space Sci. Rev., 71, 459–495, 1995.

Scudder, J. D., Cao, X., and Mozer, F. S.: Photoemission current – spacecraft voltage relation: key to routine, quantitative low-energy plasma measurements, J. Geophys. Res., 105, 21 281–21 294, 2000.

Seyler, C. E.: A mathematical model of the structure and evolution of small-scale discrete auroral arcs, J. Geophys. Res., 95, 17 199–17 215, 1990.

Stasiewicz, K., Holmgren, G., and Zanetti, L.: Density depletions and current singularities observed by Freja, J. Geophys. Res., 103, 4251–4260, 1998.

Stasiewicz, K., Khotyaintsev, Y., Berthomier, M., and Wahlund, J.-E.: Identification of widespread turbulence of dispersive Alfvén waves, Geophys. Res. Lett., 27, 173–176, 2000a.

Stasiewicz, K.: Small scale Alfvénic structure in the aurora, Space Sci. Rev., 92, 423–533, 2000b.

Streltsov, A. V. and Lotko, W.: Small-scale, "electrostatic" auroral structures and Alfvén waves, J. Geophys. Res., 104, 4411–4426, 1999.

Tung, Y.-K., Delory, G. T., and Carlson, C. W.: Modulation of auroral field-aligned electron fluxes under two inverted-V structures at different altitudes, Geophys. Res. Lett., 29, 10, doi:10.1029/2001GL013719, 2002.

Wu, C. S. and Lee, L. C.: A theory of the terrestrial kilometric radiation, Astrophys. J., 230, 621–626, 1979.

Wygant, J. R., Keiling, A., Cattell, C. A., Johnson, M., Lysak, R. L., Temerin, M., Mozer, F. S., Kletzing, C. A., Scudder, J. D., Peterson, W., Russell, C. T., Parks, G., Brittnacher, M., Germany, G., and Spann, J.: Polar spacecraft based comparisons of intense electric fields and Poynting flux near and within the plasma sheet-tail lobe boundary to UVI images: an energy source for the aurora, J. Geophys. Res., 105, 18 675–18 692, 2000.

Wygant, J. R., Keiling, A., Cattell, C. A., Lysak, R. L., Temerin, M., Mozer, F. S., Kletzing, C. A., Scudder, J. D., Streltsov, V., Lotko, W., and Russell, C. T.: Evidence for kinetic Alfvén waves and parallel electron energization at 4–6 R_E altitudes in the plasma sheet boundary layer, J. Geophys. Res., 107, A8, doi:10.1029/2001JA900113, 2002.